

Acoustic monitoring of crack formation in powder bed fusion-laser beam of CM247LC

Downloaded from: https://research.chalmers.se, 2026-11-08 05:00 UTC

Citation for the original published paper (version of record):
Vaerenberg, R., Jhabvala, J., Jamili, A. et al (2026). Acoustic monitoring of crack formation in powder bed fusion-laser beam of CM247LC. Additive Manufacturing Letters, 19. http://dx.doi.org/10.1016/j.addlet.2026.100430

N.B. When citing this work, cite the original published paper.

research.chalmers.se offers the possibility of retrieving research publications produced at Chalmers University of Technology. It covers all kind of research output: articles, dissertations, conference papers, reports etc. since 2004. research.chalmers.se is administrated and maintained by Chalmers Library

(article starts on next page)

Additive Manufacturing Letters 19 (2026) 100430

Contents lists available at ScienceDirect

Additive Manufacturing Letters

journal homepage: www.elsevier.com/locate/addlet

Short communication

Acoustic monitoring of crack formation in powder bed fusion-laser beam of CM247LC

Rik Vaerenberg [a,b,*], Jamasp Jhabvala [c], Amir Mohammad Jamili [c], Ahmed Fardan [d], Laura Perrin [c], Reza Esmaeilzadeh [c], Gowtham Soundarapandiyan [d,e], Vigneashwara Pandiyan [g,f], Roland Axel Richter [g], Federica Marone [h], Steven Van Petegem [i], Eduard Hryha [d], Roland E. Logé [c], Bey Vrancken [j,b], Konstantinos Gryllias [a,b]

[a] Department of Mechanical Engineering, Division LMSD, KU Leuven, Celestijnenlaan 300, Box 2420, Leuven, 3001, Belgium
[b] Flanders Make@KU Leuven, Leuven, Belgium
[c] Thermomechanical Metallurgy Laboratory – PX Group Chair, Ecole Polytechnique Fédérale de Lausanne (EPFL), Neuchâtel, 2002, Switzerland
[d] Department of Mechanical Engineering, Chalmers University of Technology, Göteborg, 412 96, Sweden
[e] Applied Materials Group, Laboratory for Neutron Scattering and Imaging, Paul Scherrer Institute (PSI), Villigen, Switzerland
[f] Department of Mechanical and Materials Engineering, University of Turku, Turku, 20520, Finland
[g] Laboratory for Advanced Materials Processing (LAMP), Swiss Federal Laboratories for Materials Science and Technology (Empa), Thun, Switzerland
[h] PSI Center for Photon Science, Paul Scherrer Institute (PSI), Villigen, Switzerland
[i] Structure and Mechanics of Advanced Materials, Paul Scherrer Institute (PSI), Villigen, Switzerland
[j] Department of Mechanical Engineering, Division MaPS, KU Leuven, Celestijnenlaan 300, Box 2420, Leuven, 3001, Belgium

ARTICLE INFO

Keywords:
CM247LC
Cracking
Acoustic monitoring
PBF-LB

ABSTRACT

Crack formation of CM247LC makes fabrication of this alloy by powder bed fusion-laser beam a major challenge. Rather than focusing on prevention strategies, this work investigates the possibility of monitoring crack formation using in-situ acoustic measurements. During printing, impulsive acoustic events are observed in structure-borne acoustic emission recordings, and a signal processing pipeline is proposed in order to automatically detect these events over the full print. No clear correlation was found between the number of these acoustic events and the observed crack density. However, the acoustic impulses are hypothesized to be caused by post-solidification cracks, where either the hot crack or the sharp edges of lack of fusion porosities act as initiation sites for small scale cracks. This is further validated using operando synchrotron imaging, showing that the formation of a hot crack does not seem to generate acoustic impulses, but the morphology change of the crack after solidification does. Finally, these acoustic events were not detectable with an optical microphone.

1. Introduction

Powder bed fusion-laser beam (PBF-LB) has matured into one of the most widely adopted metal additive manufacturing (AM) technologies for producing geometrically complex metallic components [1]. However, the industrial adoption of high-γ' Ni-base superalloys remains limited by their high susceptibility to cracking during PBF-LB manufacturing. Among these alloys, CM247LC is widely used in the hot sections of gas turbines owing to its excellent creep resistance and oxidation resistance, yet it is considered a very crack-susceptible non-weldable Ni-base superalloy when processed using PBF-LB [2]. Improving the understanding of crack formation and eventually its mitigation is therefore essential for enabling the reliable manufacturing and qualification of these alloys.

Cracking in PBF-LB processed Ni-base superalloys can arise through multiple mechanisms that occur at different stages of a thermal cycle. Hot cracking encompasses both solidification cracking and liquation cracking. Solidification cracking occurs during the terminal stages of solidification, where tensile stresses pull apart thin solute-rich liquid films between adjacent solidifying dendrites [2,3]. Liquation cracking, on the other hand, results from the localized melting of low-melting phases or segregation within the heat-affected zone, which then tears apart under tensile stresses [2,3]. In contrast, solid-state cracking

* Corresponding author.
E-mail address: rik.vaerenberg@kuleuven.be (R. Vaerenberg).

https://doi.org/10.1016/j.addlet.2026.100430
Received 4 September 2026; Received in revised form 9 October 2026; Accepted 21 October 2026
Available online 27 October 2026
2772-3690/© 2026 The Authors. Published by Elsevier B.V. This is an open access article under the CC BY license (http://creativecommons.org/licenses/by/4.0/).

occurs after complete solidification, either during post-solidification cooling or subsequent thermal exposure. Two commonly reported solid-state cracking mechanisms are ductility dip cracking (DDC) and strain-age cracking (SAC). DDC is generally associated with a temporary loss of ductility over a specific temperature range, whereas SAC results from the combined effect of rapid γ' precipitation and the high residual stresses retained from the PBF-LB process [2,3]. Importantly, these cracking mechanisms have distinct physical origins but are often found at dendritic and/or grain boundaries making post-mortem identification challenging.

Although hot cracking is generally accepted as the dominant cracking mechanism in as-built CM247LC, some recent studies suggest that solid-state cracking may also occur during the PBF-LB build process [4,5]. Furthermore, hot cracks are typically found at dendritic and/or grain boundaries, whereas solid-state cracking has also been reported to exhibit transgranular fracture [6].

Operando synchrotron X-ray radiography has provided insight into crack formation during PBF-LB of CM247LC. Ghasemi-Tabasi et al. [7] demonstrated that solidification and liquation cracking can be distinguished through real-time observations supported by numerical finite-element simulations. More recently, Fardan et al. [8] confirmed that cracks observed in as-built CM247LC predominantly are solidification cracking and further demonstrated crack suppression through the addition of nano-Y_2O_3 particles and Hf powder.

In addition to Fardan et al. [8], multiple other studies have been performed in order to try to reduce the cracking severity in CM247LC. First, several studies have tried changing the alloy composition, most commonly focussing on changing the Hafnium content as Hafnium has a significant influence on the solidification interval. One approach is to lower the Hafnium content in order to reduce the solidification interval to reduce the solute rich liquid in the mushy zone [9,10]. Contrary, other approaches increased the Hafnium content in order to increase the solidification range to allow for better backfilling of the incipient solidification cracks, which also reduced crack density [8,11]. Next, several studies also show that the process parameters have a significant influence on the crack formation [12–14]. Kalentics et al. [15] have also shown significant reduction of crack densities through the addition of laser shock peening. Finally, post-processing techniques such as hot isostatic pressing are also considered in order to reduce the crack density of the final part [16].

As the crack density is highly sensitive to a wide variety of parameters, there is still a need for crack detection in CM247LC. Therefore, this study assesses the possibility of monitoring the crack formation using in-situ acoustic monitoring. Previously, Seleznev et al. [17] showed the possibility of monitoring millimeter scale cracks in PBF-LB of $Al_{92}Mn_6Ce_2$ using a structure-borne sensor, which was later extended to include a machine learning approach in order to reduce the number of false positives [18]. Ito et al. [19] showed that micro-cracking can also be detected using structure-borne acoustic emission sensors. Recently, Raeker et al. [20] investigated the feasibility of using structure-borne acoustic measurements for crack detection in laser remelting in single line scans, where it was found that cold cracking causes an acoustic emission spike, while for hot cracking mechanisms no such spike was found. In contrast, Fardan et al. [8] found acoustic impulses in CM247LC printed with hot cracks while no impulses were found when the alloy was modified to eliminate the cracking.

In addition to structure-borne acoustic emissions, Moore et al. [21] showed that the cracking of a cantilever due to thermal stresses, at a designed failure point, can be monitored using an airborne microphone. In line with this, Prieto et al. [22] showed that in laser metal deposition, the internal cracks can be monitored using an optical microphone.

This work aims to investigate the possibility of using acoustic monitoring of PBF-LB for the detection of cracks in CM247LC. The crack mechanism, hot cracking or post-solidification cracking, is taken into account and both structure-borne acoustic emissions and airborne acoustic emissions are evaluated.

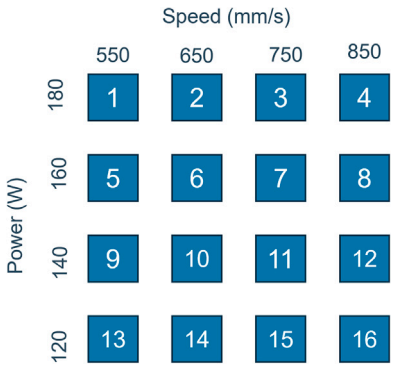


Fig. 1. Schematic of the laser speeds and powers used in the wHf and nHf experiments.

2. Materials and methods

2.1. Experimental setup

This work encompasses two experimental campaigns: an experimental campaign performed on a lab-made PBF-LB machine at EPFL and measurements performed using operando synchrotron measurements as shown in [8].

2.1.1. Measurement campaign using lab-made PBF-LB machine

The lab-made PBF-LB machine used for the experimental campaign at EPFL, as discussed in depth in [23], was equipped with a Raylase Axialscan-30 scanhead and a 1070 nm 500 W IPG laser. The beam diameter was 48 μm and the chamber was continuously flushed with Argon.

Two types of prints are considered, prints with sixteen 10 × 10 mm cubes of 1.8 mm height, and single line scans. Two sixteen-sample prints are performed: one with nominal CM247LC powder (CM247LC wHf) and one with modified powder without Hafnium, from here on called the wHf and nHf print. The powders were previously discussed in [24], with the resulting alloy composition as shown in Table 1. The goal of the sixteen-sample print was to induce different levels of cracking by changing the scan speed, laser power, and powder composition. The hatch spacing and layer height were kept constant at 60 μm and 30 μm respectively (resulting in a 60 layer print). Unidirectional scanning was employed in two configurations with a relative rotation of 90°, one scanning directly against the gas flow and one perpendicular to the gas flow. The two different scanning strategies were alternated between the layers. The speed was changed from 550 mm/s to 850 mm/s in steps of 100 mm/s, and orthogonally, the power was changed from 120 W to 180 W in steps of 20 W, which is shown schematically in Fig. 1. The resulting samples were cut from the 10 mm thick nickel baseplate using a diamond wire saw, cut in half in line with the build direction and embedded. The embedded samples were ground using fine SiC abrasive paper (2500 grit) and the surface was polished using 3 μm and 1 μm diamond paste, followed by final polishing with a non-drying OPS colloidal silica suspension.

In addition to the sixteen cube prints, a single scan line was printed directly against the gas flow on the same machine with the nominal powder, where a single line of a single layer is printed at 550 mm/s and 180 W. The printed single line was then remelted three times, using the same speed and power, as it has been shown that remelting can possibly influence the level of hot cracking [6]. The single line scan was manually ground until approximately the midpoint of the scan line and polished parallel to the laser scanning direction in order to obtain a complete microstructural overview of the entire track. The polished samples were then etched for 10 s in a boiling solution consisting of 75 mL HCl, 25 mL HNO_3, and 200 mL distilled water.

Table 1
Composition of the CM247LC powder and the modified powder without Hafnium.

wt%	Al	B	C	Co	Cr	Fe	Hf	Mo	Ni	Ta	Ti	W	Zr	O
CM247LC wHf	5.71	0.017	0.06	9.24	8.62	0.02	1.37	0.54	Bal	3.08	0.73	9.93	0.006	0.01
CM247LC nHf	5.56	0.01	0.07	9.14	8.36	0.07	0.005	0.53	Bal	3.18	0.63	9.48	0.018	0.01
CM247LC Operando	5.60	0.010	0.06	9.30	8.00	0.03	1.30	0.50	Bal	3.20	0.80	9.70	0.009	0.01

The acoustic monitoring was performed using both a structure-borne acoustic emission sensor and a XARION optical microphone. The structure-borne acoustic emission sensor was an VS370-A3 from Vallen Systeme with a frequency range from 150 kHz to 600 kHz which was mounted on the bottom of the 10 mm thick nickel baseplate. In addition to the structure-borne acoustic emission sensor, a XARION ETA 250 ultra optical microphone was installed for the wHf print, which features a bandwidth up to 1 MHz, with an integrated high-pass filter set at 10 kHz.

Both sensors were sampled at 2 MHz using an Elsys TPCE-0216-4S DAQ card, accompanied by a voltage signal from the laser card which indicated when the laser was on. For the sixteen-sample prints, the data was only analyzed starting from layer 31 (the last half of the layers) as the bottom of the cubes was removed during the cutting process and thus could not be characterized. For the nHf print, layers 40 and 59 were not analyzed as a short print interruption caused the data acquisition setup to not capture the printing of all cubes in these layers.

2.1.2. Synchrotron experiment

In addition, an experiment inside a synchrotron beamline was performed using nominal powder, CM247LC Operando in Table 1. A miniaturized PBF-LB machine was placed at an X-ray imaging beamline [25], where the top surface of a thin wall (150 μm thick) was remelted three consecutive times with a laser with a spot diameter of 50 μm, 100 W laser power and 200 mm/s scan speed. The operando X-ray imaging was conducted at the TOMCAT beamline of the Swiss Light Source (SLS), the Paul Scherrer Institute (PSI). The X-ray beam was a polychromatic beam with a peak energy of 20 keV, where, after passing through the thin wall, the X-rays were transformed into visible light through a 50 μm thick LuAG:Ce scintillator. The light was subsequently captured using a high numerical aperture microscope (4x magnification; Optique Peter, Lentilly, France) and recorded using an in-house developed GigaFRoST detector [26]. The images were captured at 10 kHz with an effective pixel size of 2.75 μm. More information of this experimental set-up can be found in Fardan et al. [8]. The obtained synchrotron video was subsequently filtered using a three point mean filter over the x,y, and time axis in order to reduce the amount of noise present. The resulting images were then finally enhanced by subtracting a Gaussian-blurred version of the image using openCV [27].

The acoustic monitoring in the synchrotron experiment was performed using the same type structure-borne acoustic emission sensor sampled at 1.5 MHz using an Advantech 1840 PCIe DAQ card. The acoustic measurement and the video were synchronized by triggering the start of the video based on the laser signal and by recording this laser signal synchronously with the acoustic emission signal.

2.2. Acoustic signal processing pipeline

Initial data observation showed clear acoustic events being present as shown in Fig. 2. Therefore, an acoustic signal processing pipeline was developed with the aim of extracting all of these events. The pipeline is based on a differentiation step, a filtering step, an enveloping step, detecting sudden energy increases and a thresholding step.

First, the signal is differentiated, as this can increase the prominence of impulsive events in acoustic signals [28] and also increased the peak values of the following proposed detector. Looking at the signal and its differentiation in Fig. 2, one can observe that next to augmenting the impulsive content, the differentiation operation has the additional benefit of removing the mean offset in the recorded AE signal.

Next, the signal is filtered with a highpass filter. Based on the short time Fourier transform (STFT) as shown in Fig. 3, the cutoff frequency was set at 200 kHz. Afterward, as the aim is to monitor the instantaneous energy of the signal, the signal is squared and lowpass filtered (at the same frequency as the highpass filter), resulting in the square envelope [29].

Now, as the goal is to detect sudden energy increases, the signal is processed by taking the difference between the acoustic energy in a window and in a subsequent non-overlapping window. This is implemented through the use of a convolutional filter in order to compute the energy difference for every time point inside the signal. However, the unnormalized energy difference gives higher values during the laser scanning. This was caused by the significantly higher acoustic energy in this segment originating from the melt pool acoustic emissions. Therefore, the energy difference between the two windows is divided by the average energy in the first window, and thus one obtains an event detector which monitors the relative change of energy between two consecutive time windows. Formally, the resulting unitless detector can be computed as follows:

$$D[i] = \frac{\sum_{k=0}^{L_w} x[i+k_1]^2 - x[i-1-k_1]^2}{\sum_{k=0}^{L_w} x[i-1-k_1]^2} \tag{1}$$

with $x[n]$ the preprocessed signal and L_w the window length. In order to determine the window length, several window lengths are compared in Fig. 4, where one can see that a window length of 250 points (0.125 ms) results in the highest value of the detector at the acoustic event in addition to having the highest peak value compared to the average value over the scan vector.

For the threshold selection, a sensitivity analysis is performed and discussed in Section 3. In addition to monitoring the threshold crossings, a hysteresis effect is built in, where the value needs to fall to the set threshold minus 5 in order to prevent multiple detections when the peak of the indicator is hovering around the threshold.

2.3. Characterization of samples printed in lab-made PBF-LB machine

The prepared cross-sections of the cubes were imaged using a Keyence Confocal microscope using twenty times magnification and images of 2048 by 1536 pixels with a corresponding pixel size of 0.34 μm by 0.34 μm. The images were then stitched using MIST stitching [30]. A section was then cut manually from the cross-section in order to obtain a rectangle as large as possible fully within the boundaries of the cross-section. The image was then converted in Python to grayscale and thresholded at a fixed pixel value of 100, where the values below this pixel value were set to zero. As care was taken to have consistent lighting conditions in the confocal microscope, this resulted in a consistent binary image for all the samples. Then, a binary closing operation was performed with a disk footprint with a radius of 5 pixels. The closing operation was added as it was observed that without this closing operation a single crack would be segmented in different segments. Following this, the binary image was divided into its distinct continuous regions. The obtained regions were filtered based on three criteria in order to retain only the cracks and exclude other voids due to porosities induced during printing. First, a minimum pixel area of 4 was enforced in order to remove single pixel outliers. Then the ratio of the major and minor axes was set to a minimum of five to only retain the thin regions [31]. Finally, the regions needed to have a minimum angle of 10 degrees with respect to the horizontal axis, as the cracks

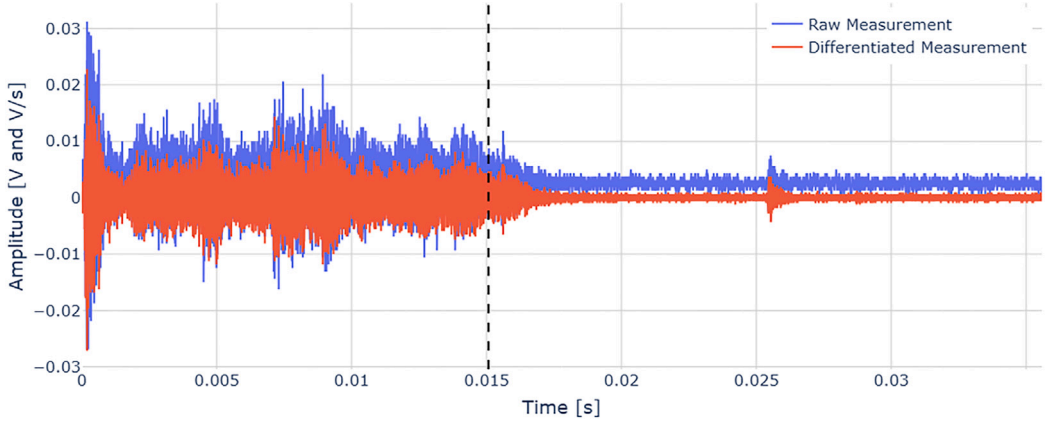


Fig. 2. Measurement of scan vector 21 of layer 31 of sample 6 in the nHf print. Dashed line indicating when the laser turned off.

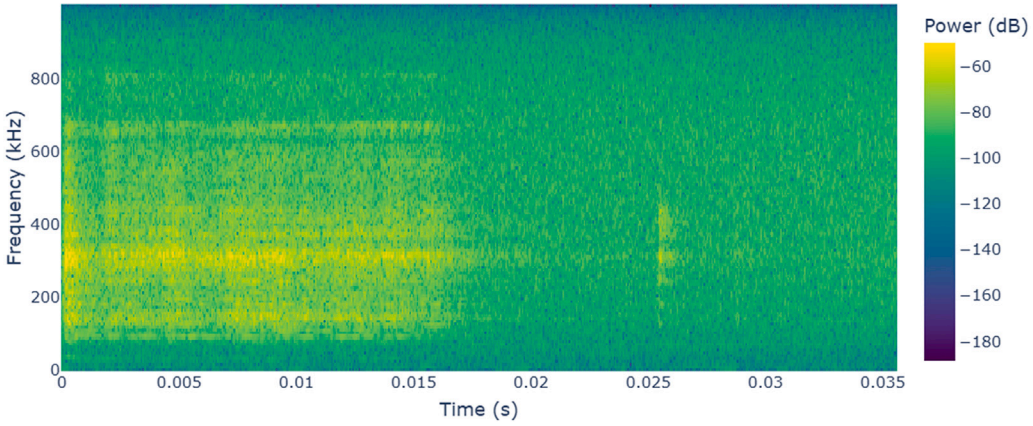
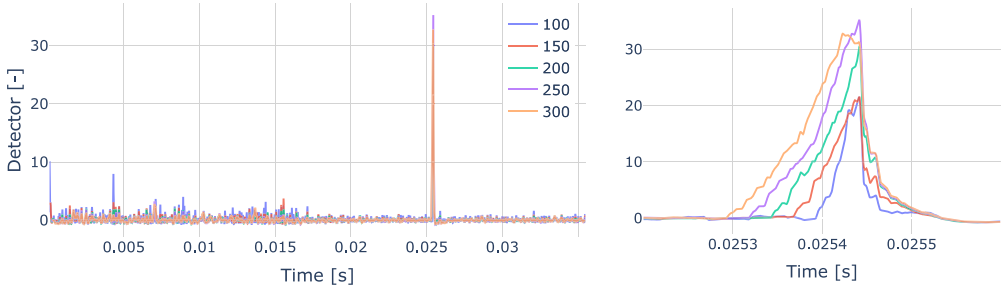


Fig. 3. STFT of the differentiated measurement of scan vector 21 of layer 31 of sample 6 in the nHf print.



(a) Full scan line. (b) Zoomed in

Fig. 4. The proposed detector, of scan vector 21 of layer 31 of sample 6 in the nHf print, with different filter lengths.

are expected to be in line with the build direction and the horizontal thin sections are likely lack of fusion porosities [10]. The result of this operation for a zoom of the cross-section of nHf sample 4 is shown in Fig. B.15. Note that the cracks connected to the porosities are not quantified, as in the optical images it is ambiguous where the porosity ends and where the crack starts.

Finally, the lengths of all major axes of all segmented cracks are summed (in mm) and divided by the surface area of the cross-section (in mm^2) in order to obtain the crack density (in mm/mm^2).

In addition to the confocal microscope, the samples were also characterized using a Zeiss Gemini 450 scanning electron microscope (SEM) equipped with an Electron Backscatter Diffraction (EBSD) detector (CMOS Symmetry camera, Oxford Instruments). EBSD maps were acquired with a step size of 86.3 nm scanning an area of 513*481 pixels with a hit rate of 89.5%, where the lower hit rate is caused by the porosity and cracks in the image. Accelerating voltage and working distance were 20 KeV and 13.9 mm respectively. The exposure time for EBSD detector was set to 6 ms. The raw EBSD data were processed using AztecCrystal software, applying standard cleanup procedures that modified less than 10% of the original data points.

3. Results and discussion

The first results shown in Fig. 6(a) give the detected cracks for every sample in the nHf and wHf with respect to the normalized enthalpy, based on the normalized enthalpy calculation of [10]. Note that, while on average the nHf print did have a reduced observed crack density, the choice of speed and power seems to have a larger influence than

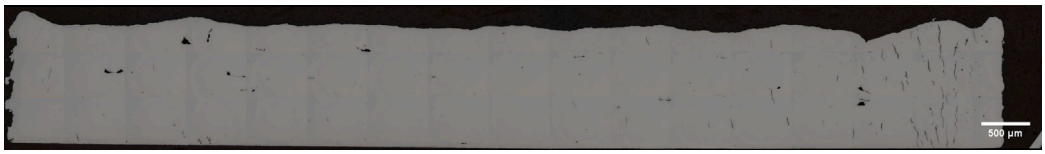
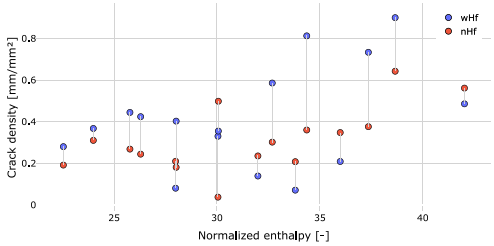
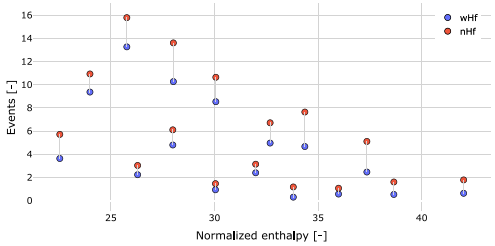


Fig. 5. Cross-section of sample 1 of the wHf test.

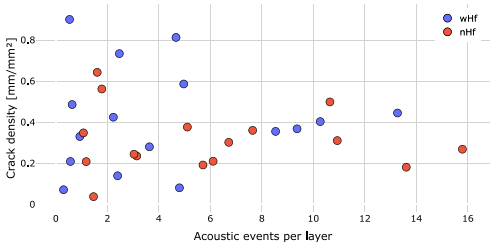


(a) Normalized enthalpy in function of crack density.

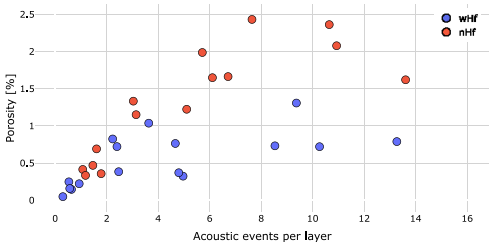


(b) Normalized enthalpy in function of acoustic events.

Fig. 6. The relation between the normalized enthalpy and the observed crack density and average acoustic emission events per layer.



(a) The observed crack density in function of the number of detected acoustic events per layer.



(b) The optically observed porosity in function of the number of detected acoustic events.

Fig. 7. The relation between the number of acoustic events and the results from the optical images where each point represents a different cube using different process parameters.

the alloy modification [32,33]. Interestingly, the crack density was also greater at the right-hand side of the cross-section as illustrated in Fig. 5, which corresponded to the start of the scan vectors that were parallel to the cross-section. Note that the chosen scan strategy resulted in alternating layers with scan vectors going right to left and coming out of the image plane. In addition, Fig. 6(b) shows the normalized enthalpy in function of average number of acoustic events per layer, with a threshold on the detector (1) output set at a value of 15. From these figures, no clear correlation can be seen initially.

In order to validate this, the observed crack density is compared against the number of acoustic events per layer across the different cubes in Fig. 7(a). The correlation between the two shows a Spearman correlation coefficient of 0.005 and an associated p-value (with a null hypothesis of them being uncorrelated and the alternative of them being positively correlated) of 0.976 [34]. Therefore, it can be concluded that there is no correlation found between the observed crack density and acoustic events. Note that the two datasets are considered together, as the same type of cracking is observed. However, even when considering the datasets separately, there is also no significant correlation found.

Observing the cross-sections using SEM, the detected cracks using optical microscopy were investigated showing indeed hot crack characteristics such as the dendritic-like crack surface as can be seen in Fig. 8.

As no correlation was found, the impulsive acoustic events are unlikely to be generated by the hot cracking initiation. This could be expected given that these acoustic events occur several milliseconds

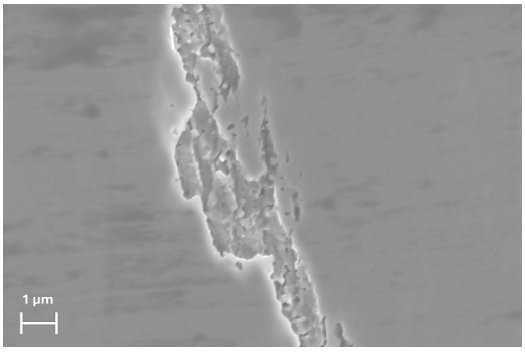
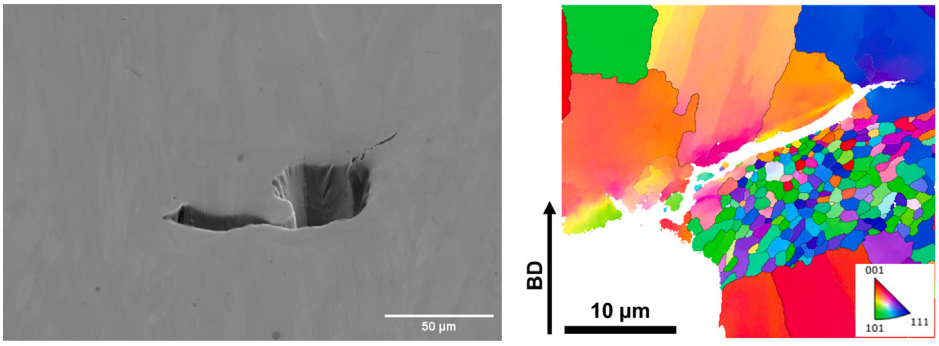


Fig. 8. Observed crack in sample 1 of the nHf print.

after the scan line is finished, as observed in Fig. 2, and thus most of the scan line is already fully solidified. The question then arises what the origin is of these impulsive events.

In addition to these hot cracks, smaller cracks were also observed at the edge of porosities. One such crack is shown in Fig. 9(a). When visualizing the grains using EBSD, as shown in Fig. 9(b), it can also be observed that the crack goes through the grain. As the hot cracking mechanisms observed in CM247LC, liquation and solidification cracking, only occur at grain boundaries, the observed crack is likely a crack that occurred post-solidification. However, the size of the cracks



(a) An observed crack using SEM at the edge of a pore.

(b) EBSD map of the crack at the edge of a pore.

Fig. 9. A porosity-connected transgranular crack.

relative to the porosity and the fact that they are connected to the porosity, prevents the optical characterization of the cross-section from detecting these cracks.

Instead, the total porosity, which captures both the lack of fusion pores and the larger-scale hot cracks, as quantified by the number of dark pixels after thresholding, is shown as a function of the acoustic events in Fig. 7(b). With a Spearman correlation of 0.752 and an associated p-value of 6.9×10^{-7}, there is a clear correlation between the porosity level and the acoustic events [34]. Therefore, a possible explanation for the acoustic events are post-solidification cracking phenomena during printing instead of the hot cracks observed in the optical images, where the sharp edges of the lack of fusion porosities and the previously existing hot cracks act as an initiation site for the formation of cracks after solidification.

In line with these results, Raeker et al. [20] investigated acoustic emissions of crack formation in laser melting of CMSX-4 and TZM, where CMSX-4 exhibited hot cracks and TZM exhibited cold cracks. They also observed that hot cracks in CMSX-4 did not generate impulsive acoustic signatures recorded by a structure-borne acoustic emission sensor, while the cold cracks in TZM did. It can be hypothesized that this is due to the fact that there is little stress build up in hot cracking, the liquid present when hot cracks are formed cannot withstand significant levels of stress and thus the opening of the liquid is likely to not generate a significant stress wave.

Additionally, two single line experiments were performed in order to verify that the initial formation of the hot cracks does not cause these acoustic emission spikes. The first experiment considered is the synchrotron experiment as shown in Fig. 10. During the scanning the acoustic signal is dominated by the melt pool signal and no clear events can be observed, despite numerous hot cracks forming. Right after the laser turns off, it is observed that a hot crack still gets formed at the end of the scan line as shown in the first two images in Fig. 10(c). These hot cracks were formed at the edge of the solidifying melt pool at the leftmost edge of the scan. The formation of these hot cracks at the edge allowed for the investigation of the acoustic signatures of the formation of a hot crack without the laser active. However, both in the raw signal in Fig. 10(a) and in the STFT in Fig. 10(b) no clear acoustic signature can be observed. Later, a first impulsive event can be observed, and in parallel it was found that one of the previously formed hot cracks had a significant change in its morphology. As this area of the scan line was further away from the edge and should therefore already be fully solidified, it is hypothesized that the previously formed hot crack propagated further after solidification.

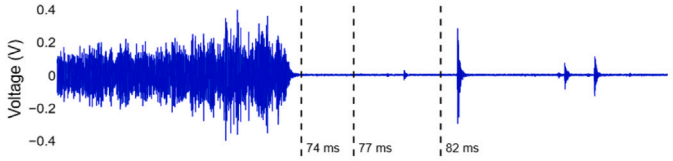
To verify these same conclusions hold in the machine used for the cube print, a single scan track experiment was performed on the same machine as the cube prints. The printed scan line was remelted three times in order to induce hot cracking [6], sectioned longitudinally, and imaged using SEM as shown in Fig. 11. Some cracking is visible in this scan line, but no acoustic events were recorded in the structure-borne acoustic emissions. All the acoustic emissions of the remelting experiment are visualized in Appendix A.

Table 2
Spearman correlation coefficients between the number of acoustic events and porosity or crack density as a function of detection threshold.

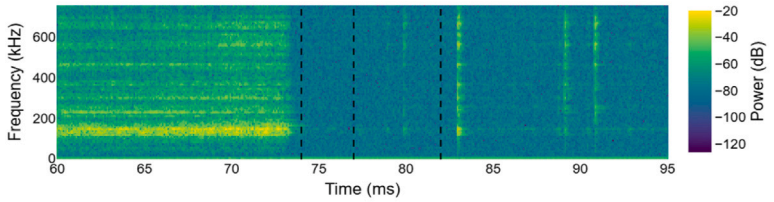
Threshold	Porosity	Crack density
7.5	0.749	−0.006
10.0	0.759	−0.007
12.5	0.751	0.009
15.0	0.752	0.005
17.5	0.755	0.006
20.0	0.752	0.008

Finally, in order to verify that these findings are not related to the specific chosen threshold, the Spearman correlation coefficients were evaluated for a wide range of thresholds as shown in Table 2. It can be clearly seen that for a wide range of thresholds, the same conclusions hold. In addition to the values reported in the table, a separate experiment was run with a threshold at a factor of 2 and requiring a drop below 1.5 in order to detect the next one. This experiment resulted in a Spearman correlation coefficient of 0.250 between the acoustic events and the crack formation and −0.161 between the acoustic events and the porosities. Therefore, one can conclude that the results obtained were consistent as long as the threshold is put high enough to not have excessive false positives due to the melt pool acoustic emissions.

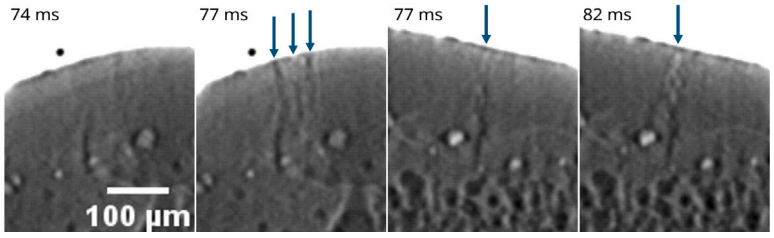
In addition to the structure-borne acoustic emission sensor, a XARION optical microphone was also present in the wHf print. The combination of the two signals (after z-normalization for illustrative purposes) is shown in Fig. 12. Note that after the scanning, there is a clear impulsive event in the structure-borne recording around time point 16 ms, which is not visible in the microphone data. When looking at the STFT of the two signals, as shown in Fig. 13, the same conclusion can be drawn: while the microphone carries information when the melt pool is active, the event present after the laser turned off is not visible in the microphone recording. When applying the previously proposed signal processing pipeline to the microphone signal (using the initial threshold of 15) one detects five events over the full wHf print. All five detected events occurred during the scanning and could therefore be caused by sudden changes in vapor gas generation [35]. It is therefore hypothesized that the microphone is unable to detect these acoustic events due to the combination of the bad coupling of the subsurface events with the airborne signal [35] and the scale of the transgranular cracks as shown in Fig. 9(a). Note that the previous studies showing the possibility of monitoring the formation of cracks using airborne signals were investigating larger scale cracks [21,22].



(a) Raw recorded signal.



(b) STFT of the recorded signal.



(c) Synchrotron images showing the hot cracking occurring between 74 ms and 77 ms and the morphology of a different crack at a different location in the scan line changing between 77 ms and 82 ms. Arrows indicating the hot cracking.

Fig. 10. The relation between the measured acoustic emissions and operando synchrotron imaging where the top surface was scanned three times, with the final scan going right to left.



Fig. 11. Zoomed-in section of the stitched SEM image of a longitudinally cross-sectioned single line track which was remelted three times on the in-house machine.

4. Conclusion

This work investigates the possibility of monitoring crack formation in CM247LC using acoustic emission monitoring. Several experiments were performed: sixteen-sample cube prints both with unmodified and modified powder without Hafnium and single line scans with unmodified powder. Clear impulsive events are detected in the structure-borne acoustic emission sensor recordings, and a signal processing pipeline is proposed to detect these events automatically.

No correlation was found between the impulsive acoustic events and the crack densities quantified using optical microscopy. However, a clear correlation was found between the total porosity, caused by the lack of fusion pores and the hot cracks, and the number of acoustic emission events. In addition, transgranular cracks were observed at the sharp edges of these porosities resulting in the hypothesis that these acoustic events are generated through post-solidification cracking mechanisms. In order to verify these conclusions, single line scan experiments were performed, including one with operando synchrotron imaging, showing no clear impulsive events for hot cracking. However, based on the presented results, one cannot conclude that post-solidification cracks are the only cause of the impulsive events. These conclusions remained consistent over a wide range of considered thresholds for the crack detection mechanism. Furthermore, the use of an optical microphone is investigated, where the acoustic events that were visible in the structure-borne acoustic emission sensor were not visible in the microphone recording, likely due to the small scale of the post-solidification cracks.

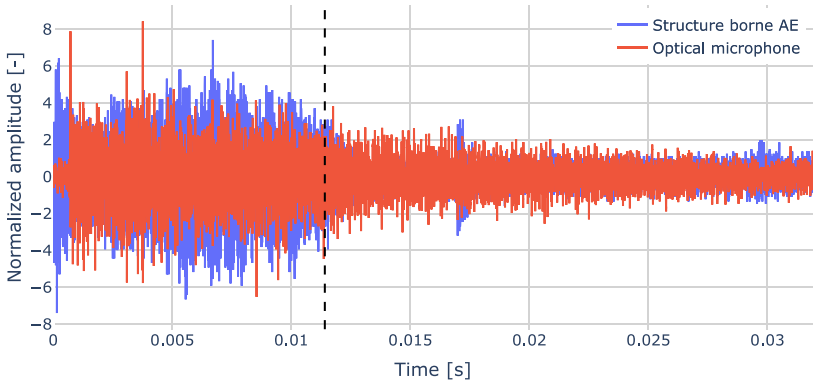
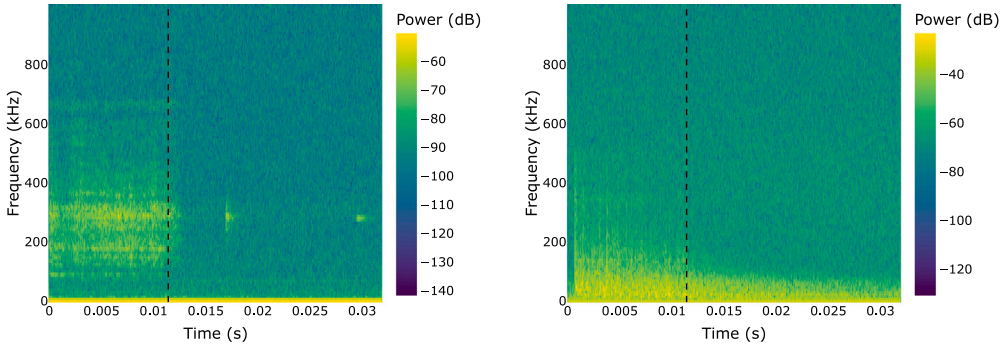


Fig. 12. Structure-borne acoustic emissions and microphone recording of scan vector 121 of layer 40 of sample 8 in the wHf print with dashed black line indicating when the laser turned off. Signals normalized for visualization purposes.



(a) STFT of the structure-borne acoustic emission recording.

(b) STFT of the optical microphone recording.

Fig. 13. STFT of scan vector 121 of layer 40 of sample 8 in the wHf print, black dashed line indicating the time the laser turned off.

CRediT authorship contribution statement

Rik Vaerenberg: Writing – review & editing, Writing – original draft, Visualization, Software, Project administration, Methodology, Investigation, Funding acquisition, Formal analysis, Data curation, Conceptualization. **Jamasp Jhabvala:** Writing – review & editing, Supervision, Resources, Project administration, Methodology, Investigation, Data curation, Conceptualization. **Amir Mohammad Jamili:** Writing – review & editing, Writing – original draft, Visualization, Investigation, Formal analysis. **Ahmed Fardan:** Writing – review & editing, Writing – original draft, Investigation, Formal analysis. **Laura Perrin:** Investigation. **Reza Esmaeilzadeh:** Investigation. **Gowtham Soundarapandiyan:** Writing – review & editing, Investigation, Formal analysis. **Vigneashwara Pandiyan:** Writing – review & editing, Investigation, Formal analysis, Data curation. **Roland Axel Richter:** Writing – review & editing, Investigation. **Federica Marone:** Writing – review & editing, Formal analysis. **Steven Van Petegem:** Writing – review & editing, Resources, Investigation. **Eduard Hryha:** Writing – review & editing, Supervision, Project administration. **Roland E. Logé:** Writing – review & editing, Supervision, Resources, Project administration, Funding acquisition, Conceptualization. **Bey Vrancken:** Writing – review & editing, Supervision, Project administration, Funding acquisition. **Konstantinos Gryllias:** Writing – review & editing, Supervision, Project administration, Funding acquisition.

Declaration of competing interest

The authors declare that they have no known competing financial interests or personal relationships that could have appeared to influence the work reported in this paper.

Acknowledgments

This research was partially supported by Flanders Make, the strategic research center for the manufacturing industry via the MUSIC SBO project. The authors would also like to acknowledge the financial support of the Internal KU Leuven Funds. In addition, Rik Vaerenberg would like to acknowledge the FWO SBO fellowship program (project number: 1SE9325N) and the FWO Travel grant (grant number: V445325N).

Ahmed Fardan, Gowtham Soundarapandiyan and Eduard Hryha acknowledge Swedish Governmental Agency for Innovation Systems (Vinnova) for funding through MAGDA (Materials for green hydrogen fueled gas turbines through additive manufacturing) project and the Centre for Additive Manufacturing – Metal (CAM^2).

Gowtham Soundarapandiyan and Steven Van Petegem acknowledge the PSI CROSS project "Enabling Acoustic Emission for monitoring Selective Laser Melting guided by in situ synchrotron X-ray diffraction experiments". The Paul Scherrer Institute is acknowledged for provision of X-ray beam time at the TOMCAT beamline (proposal No. 20220659).

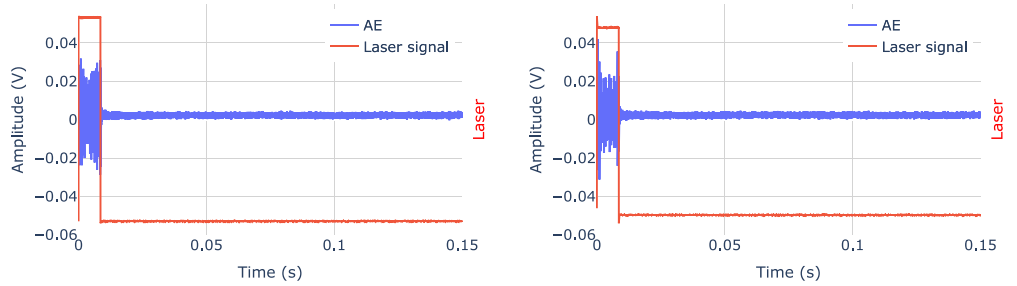
Finally, Steven Van Petegem is grateful for financial support from the Swiss National Science Foundation under grant 193799.

Appendix A. Structure-borne acoustic emissions for single-scan remelting

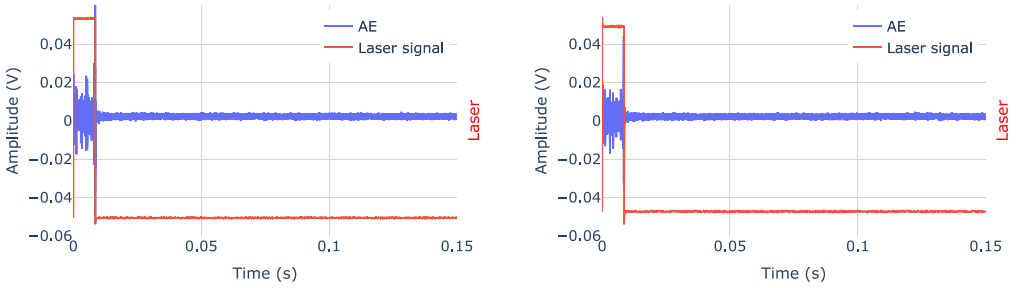
See Fig. A.14.

Appendix B. Optical image analysis

See Fig. B.15.



(a) Initial scan (b) First remelting



(c) Second remelting (d) Third remelting

Fig. A.14. Structure-borne recordings of the single line experiment.

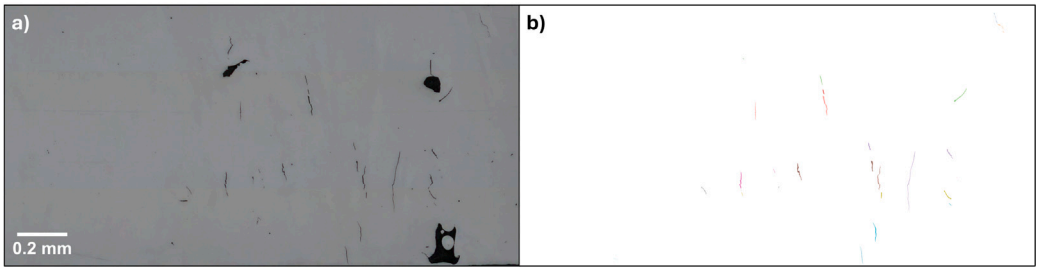
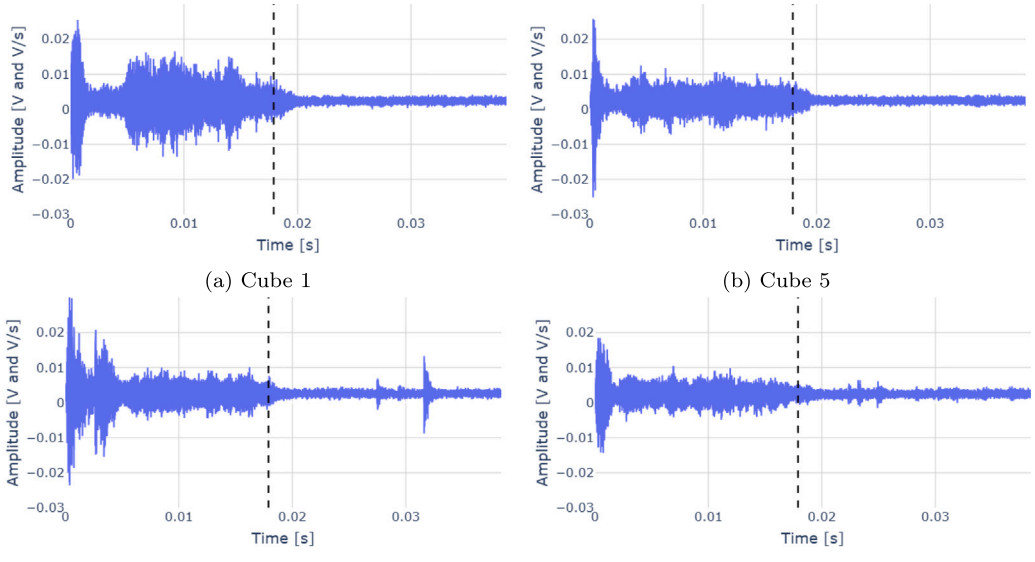


Fig. B.15. The image processing pipeline applied on a zoom of the cross-section of nHf sample 4. (a) a zoom of the greyscale image. (b) the resulting segmented cracks.



(a) Cube 1 (b) Cube 5

(c) Cube 9 (d) Cube 13

Fig. C.16. Effect of changing laser power, 180 W in cube 1 to 120 W in cube 13, on the melt pool acoustic emissions, for scan line 61 in layer 40. Dashed black line indicating when the laser is turned off.

Appendix C. Effect of laser power on melt pool acoustic emissions

Fig. C.16 shows the effect of laser power on the acoustic emissions when the melt pool is active, where the measured signal energy when the laser is active drops from 30 $\frac{V^2}{s}$ in cube 1 to 18 $\frac{V^2}{s}$ in cube 13.

References

[1] T. DebRoy, H.L. Wei, J.S. Zuback, T. Mukherjee, J.W. Elmer, J.O. Milewski, A.M. Beese, A.d. Wilson-Heid, A. De, W. Zhang, Additive manufacturing of metallic components–process, structure and properties, Prog. Mater. Sci. 92 (2018) 112–224, http://dx.doi.org/10.1016/j.pmatsci.2017.10.001.

[2] P.D. Enrique, T. Minasyan, E. Toyserkani, Laser powder bed fusion of difficult-to-print γ' Ni-based superalloys: a review of processing approaches, properties, and remaining challenges, Addit. Manuf. (2025) 104811, http://dx.doi.org/10.1016/j.addma.2025.104811.

[3] J. Xu, P. Kontis, R.L. Peng, J. Moverare, Modelling of additive manufacturability of nickel-based superalloys for laser powder bed fusion, Acta Mater. (ISSN: 13596454) 240 (2022) 118307, http://dx.doi.org/10.1016/j.actamat.2022.118307.

[4] J.N. Ghoussoub, Y.T. Tang, W.J.B. Dick-Cleland, A.A.N. Németh, Y. Gong, D.G. McCartney, A.C.F. Cocks, R.C. Reed, On the influence of alloy composition on the additive manufacturability of Ni-Based superalloys, Met. Mater. Trans. A (ISSN: 1543-1940) 53 (3) (2022) 962–983, http://dx.doi.org/10.1007/s11661-021-06568-z.

[5] K. Guo, S. Xu, L. Zhao, R. Zhao, Y. Hou, J. Wang, C. Chen, Z. Ren, Cracking behavior in laser powder bed fusion of non-weldable Ni-based superalloys: A multi-physics numerical and experimental study, Addit. Manuf. (ISSN: 2214-8604) 126 (2026) 105264, http://dx.doi.org/10.1016/j.addma.2026.105264.

[6] Y. Shi, A. Wu, S. Li, L. Shi, L. Lei, L. Shi, W. Li, X. Su, Crack mitigation in selective laser melting of CM247LC superalloy via post-heating laser tracks: Influence on microstructure and cracking behavior, Mater. Charact. (2025) 115117, http://dx.doi.org/10.1016/j.matchar.2025.115117.

[7] H. Ghasemi-Tabasi, C. de Formanoir, S. Van Petegem, J. Jhabvala, S. Hocine, E. Boillat, N. Sohrabi, F. Marone, D. Grolimund, H. Van Swygenhoven, et al., Direct observation of crack formation mechanisms with operando laser powder bed fusion X-ray imaging, Addit. Manuf. 51 (2022) 102619, http://dx.doi.org/10.1016/j.addma.2022.102619.

[8] A. Fardan, G. Soundarapandiyan, V. Pandiyan, S. Van Petegem, E. Polatidis, S. Kazi, S. Goel, C. Pauzon, F. Marone, B. Mehta, A. Parrilli, H. Brodin, E. Hryha, Unveiling crack mitigation pathways in powder bed fusion–laser beam of CM247LC: an operando X-ray radiography study of Hf and nano-Y2O3 additions, Prog. Addit. Manuf. (ISSN: 2363-9520) (2026) http://dx.doi.org/10.1007/s40964-026-01876-5.

[9] P. Hu, Z. Liu, M. Chen, Y. Li, X. Qi, J. Xie, Reducing cracking sensitivity of CM247lc processed via laser powder bed fusion through composition modification, 2024, http://dx.doi.org/10.1016/j.jmrt.2024.02.082, Available at SSRN 4658186.

[10] S. Griffiths, H.G. Tabasi, T. Ivas, X. Maeder, A. De Luca, K. Zweiacker, R. Wróbel, J. Jhabvala, R. Logé, C. Leinenbach, Combining alloy and process modification for micro-crack mitigation in an additively manufactured Ni-base superalloy, Addit. Manuf. 36 (2020) 101443, http://dx.doi.org/10.1016/j.addma.2020.101443.

[11] R. Engeli, Selective Laser Melting & Heat Treatment of Γ Strengthened Ni-Base Superalloys for High Temperature Applications (Ph.D. thesis), ETH Zurich, 2017, http://dx.doi.org/10.3929/ethz-b-000000074.

[12] L.N. Carter, C. Martin, P.J. Withers, M.M. Attallah, The influence of the laser scan strategy on grain structure and cracking behaviour in SLM powder-bed fabricated nickel superalloy, J. Alloys Compd. 615 (2014) 338–347, http://dx.doi.org/10.1016/j.jallcom.2014.06.172.

[13] S. Catchpole-Smith, N. Aboulkhair, L. Parry, C. Tuck, I.A. Ashcroft, A. Clare, Fractal scan strategies for selective laser melting of 'unweldable'nickel superalloys, Addit. Manuf. 15 (2017) 113–122.

[14] O. Adegoke, J. Andersson, H. Brodin, R. Pederson, P. Harlin, Influence of laser powder bed fusion process parameters on the microstructure and cracking susceptibility of nickel-based superalloy alloy 247lc, Results Mater. 13 (2022) 100256.

[15] N. Kalentics, N. Sohrabi, H.G. Tabasi, S. Griffiths, J. Jhabvala, C. Leinenbach, A. Burn, R.E. Loge, Healing cracks in selective laser melting by 3D laser shock peening, Addit. Manuf. 30 (2019) 100881, http://dx.doi.org/10.1016/j.addma.2019.100881.

[16] L.N. Carter, M.M. Attallah, R.C. Reed, et al., Laser powder bed fabrication of nickel-base superalloys: influence of parameters; characterisation, quantification and mitigation of cracking, Superalloys 2012 (6) (2012) 2826–2834.

[17] M. Seleznev, T. Gustmann, J.M. Friebel, U.A. Peuker, U. Kühn, J.K. Hufenbach, H. Biermann, A. Weidner, In situ detection of cracks during laser powder bed fusion using acoustic emission monitoring, Addit. Manuf. Lett. 3 (2022) 100099, http://dx.doi.org/10.1016/j.addlet.2022.100099.

[18] D.Y. Kononenko, V. Nikonova, M. Seleznev, J. van den Brink, D. Chernyavsky, An in situ crack detection approach in additive manufacturing based on acoustic emission and machine learning, Addit. Manuf. Lett. 5 (2023) 100130, http://dx.doi.org/10.1016/j.addlet.2023.100130.

[19] K. Ito, M. Kusano, M. Demura, M. Watanabe, Detection and location of microdefects during selective laser melting by wireless acoustic emission measurement, Addit. Manuf. 40 (2021) 101915, http://dx.doi.org/10.1016/j.addma.2021.101915.

[20] E.B. Raeker, N. Tulshibagwale, K.M. Mullin, J.D. Lamb, T.M. Pollock, Detection and classification of cracking via acoustic emission during Laser-Melting screening for additive manufacturing: Raeker, Tulshibagwale, Mullin, Lamb, and Pollock, JOM 77 (10) (2025) 7274–7286, http://dx.doi.org/10.1007/s11837-025-07642-2.

[21] K. Moore, D. Kouprianoff, D. Louw, I. Yadroitsava, I. Yadroitsev, Monitoring for cracks in metal l-pbf using gas-borne acoustic emission, South Afr. J. Ind. Eng. 34 (4) (2023) 147–154.

[22] C. Prieto, R. Fernandez, C. Gonzalez, M. Diez, J. Arias, R. Sommerhuber, F. Lücking, In situ process monitoring by optical microphone for crack detection in laser metal deposition applications, in: 11th CIRP Conference on Photonic Technologies [LANE 2020], 2020.

[23] A.M. Jamili, J. Jhabvala, S. Van Petegem, D. Weisz-Patrault, E. Boillat, J. Nohava, A. Özsoy, S. Banait, N. Casati, R.E. Logé, Avoiding cracks in multi-material printing by combining laser powder bed fusion with metallic foils: Application to Ti6Al4V-AlSi12 structures, Addit. Manuf. 97 (2025) 104615, http://dx.doi.org/10.1016/j.addma.2024.104615.

[24] S. Griffiths, H. Ghasemi-Tabasi, A. De Luca, J. Pado, S.S. Joglekar, J. Jhabvala, R.E. Logé, C. Leinenbach, Influence of Hf on the heat treatment response of additively manufactured Ni-base superalloy CM247LC, Mater. Charact. 171 (2021) 110815, http://dx.doi.org/10.1016/j.matchar.2020.110815.

[25] S. Hocine, S. Van Petegem, U. Frommherz, G. Tinti, N. Casati, D. Grolimund, H. Van Swygenhoven, A miniaturized selective laser melting device for operando X-ray diffraction studies, Addit. Manuf. 34 (2020) 101194, http://dx.doi.org/10.1016/j.addma.2020.101194.

[26] R. Mokso, C.M. Schlepütz, G. Theidel, H. Billich, E. Schmid, T. Celcer, G. Mikuljan, L. Sala, F. Marone, N. Schlumpf, M. Stampanoni, GigaFRoST: the gigabit fast readout system for tomography, Synchrotron Radiat. 24 (6) (2017) 1250–1259, http://dx.doi.org/10.1107/S1600577517013522.

[27] G. Bradski, The OpenCV library, Dr. Dobb's J. Softw. Tools (2000).

[28] I. Kauppinen, Methods for detecting impulsive noise in speech and audio signals, in: 2002 14th International Conference on Digital Signal Processing Proceedings. DSP 2002 (Cat. No. 02TH8628), Vol. 2, IEEE, 2002, pp. 967–970, http://dx.doi.org/10.1109/ICDSP.2002.1028251.

[29] J.G. Proakis, M. Salehi, Digital Communications, vol. 4, McGraw-hill New York, 2001.

[30] J. Chalfoun, M. Majurski, T. Blattner, K. Bhadriraju, W. Keyrouz, P. Bajcsy, M. Brady, MIST: accurate and scalable microscopy image stitching tool with stage modeling and error minimization, Sci. Rep. 7 (1) (2017) 4988, http://dx.doi.org/10.1038/s41598-017-04567-y.

[31] A. Ardeshiri, S.H. Razavi, M. Khodabakhshi, R. Ashiri, Optimization and insights toward fully dense crack-free additive manufacturing of Hastelloy-X by selective laser melting technology, J. Mater. Res. Technol. (2025) http://dx.doi.org/10.1016/j.jmrt.2025.10.061.

[32] A. Fardan, A. Fazi, R.L. Peng, T. Mishurova, M. Thuvander, G. Bruno, H. akan Brodin, E. Hryha, Fine-Tuning melt pools and microstructures: Taming cracks in powder bed fusion—Laser beam of a non-weldable Ni-base superalloy, Materialia (ISSN: 2589-1529) 34 (2024) 102059, http://dx.doi.org/10.1016/j.mtla.2024.102059.

[33] A. Fardan, J. Schröder, J. Xu, H. Brodin, E. Hryha, Role of scan strategies in modulating micro and macro-cracking in CM247LC processed by powder bed fusion–laser beam, Prog. Addit. Manuf. (ISSN: 2363-9520) 11 (6) (2026) 6235–6251, http://dx.doi.org/10.1007/s40964-026-01701-z.

[34] C. Spearman, The proof and measurement of association between two things, Am. J. Psychol. (1987) http://dx.doi.org/10.2307/1422689.

[35] Y. Sun, S. Gorgannejad, A. Martin, J. Nicolino, M. Strantza, J.-B. Forien, V. Thampy, S. Liu, P. Quan, C.J. Tassone, et al., Direct mechanistic connection between acoustic signals and melt pool morphology during laser powder bed fusion, Appl. Phys. Lett. 125 (3) (2024) http://dx.doi.org/10.1063/5.0205663.